

MFogHub: Bridging Multi-Regional and Multi-Satellite Data for Global Marine Fog Detection and Forecasting

Anonymous CVPR submission

Paper ID 8175

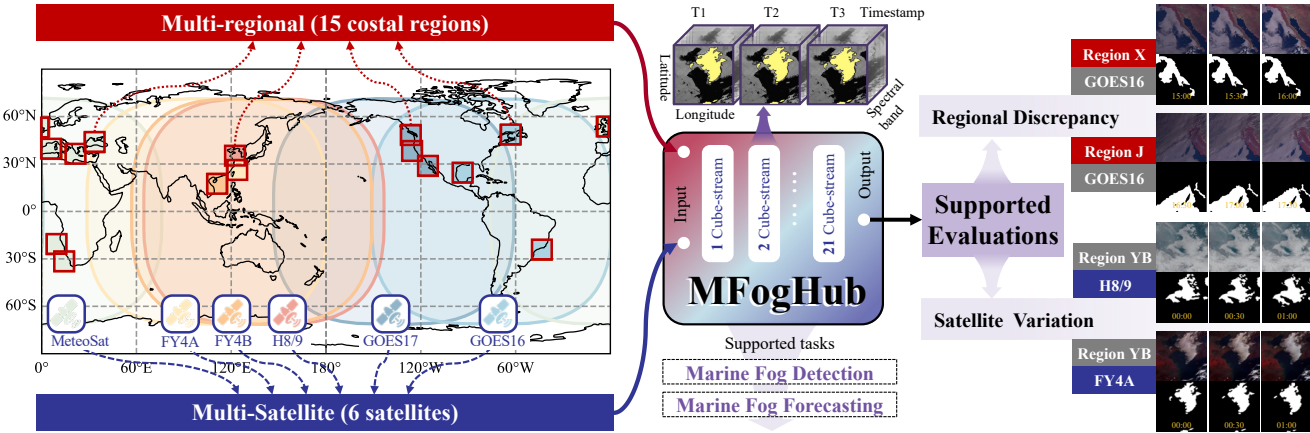


Figure 1. Overview of MFogHub. **Right:** MFogHub collects data from 15 marine fog-prone regions worldwide, captured by 6 geostationary satellites. **Middle:** Data for each region-satellite pair is organized in a cube-stream structure with dimensions of “timestamp-spectral band-latitude-longitude.” MFogHub includes 21 cube-streams in total, each with corresponding masks, supporting both detection and forecasting tasks. **Left:** MFogHub enables unique evaluations of model generalization across multiple regions and satellite.

Abstract

Deep learning approaches for marine fog detection and forecasting have outperformed traditional methods, demonstrating significant scientific and practical importance. However, the limited availability of open-source datasets remains a major challenge. Existing datasets, often focused on a single region or satellite, restrict the ability to evaluate model performance across diverse conditions and hinder the exploration of intrinsic marine fog characteristics. To address these limitations, we introduce **MFogHub**, the first multi-regional and multi-satellite dataset to integrate annotated marine fog observations from 15 coastal fog-prone regions and six geostationary satellites, comprising over 68,000 high-resolution samples. By encompassing diverse regions and satellite perspectives, MFogHub facilitates rigorous evaluation of both detection and forecasting methods under varying conditions. Extensive experiments with 16 baseline models demonstrate that MFogHub can reveal generalization fluctuations due to regional and satellite discrepancy, while also serving as a valuable resource for the development of targeted and scalable fog prediction

techniques. Through MFogHub, we aim to advance both the practical monitoring and scientific understanding of marine fog dynamics on a global scale. The dataset and code are available in the supplementary materials.

1. Introduction

Marine fog is a complex and hazardous meteorological phenomenon that occurs in the lower atmosphere over oceanic regions [15, 16]. During the marine fog formation process, horizontal visibility often drops below one kilometer [12, 23], causing significant disruptions to shipping, port operations, and coastal activities [2, 25]. As such, research on marine fog detection and forecasting is of both scientific and practical importance.

In recent years, data-driven deep learning methods [3, 8, 20, 43] have increasingly outperformed traditional approaches [10, 33, 42] in marine fog detection and forecasting. However, as shown in Table 1, the limited availability of open-source datasets in this area has led most studies [3, 13, 19, 21, 22, 24, 39, 43] to rely on region-specific or satellite-specific data collected in isolation. Consequently,

021
022
023
024

025

026
027
028
029
030
031
032
033

034
035
036
037
038
039
040

Table 1. Comparisons with existing marine fog detection and forecasting benchmarks: detailed overview of dataset information, geographic coverage, satellite types, event counts, supported tasks, and open accessibility. (C_{sat} represents the number of spectral bands for different satellites, e.g. $C_{FY4A} = 14$, $C_{H8/9} = 16$)

Datasets	Information			Regions	Satellites	Events	Tasks	Open					
	Num.	Size ($H \times W$)	Spectral bands	Pixel-level labels	Num.	Name	Num.	Types	w/w.o.	Num.	Detection	Prediction	
Nilo et al. (2018) [24]	72	-	-	X	1	Seas off Italy	1	MeteoSat	✓	9	✓	X	X
Huang et al. (2021) [3]	201	(1024,1024)	16	✓	1	Yellow and Bohai Sea	1	H8/9	✓	-	✓	X	X
Mahdavi et al. (2020) [21]	53	-	-	X	1	The Grand Banks	1	GOES	✓	26	✓	X	X
Zhou et al. (2022) [43]	1,040	(512,512)	3	✓	1	Yellow and Bohai Sea	1	GOCI	✓	133	✓	X	✓
Tao et al. (2022) [19]	1,100	(64,64)	16	X	1	Yellow and Bohai Sea	1	H8/9	X	-	✓	X	X
Huang et al. (2023) [13]	4,291	(1024, 1024)	3	(356)	1	Yellow and Bohai Sea	1	H8/9	✓	-	✓	X	✓
Su et al. (2023) [29]	1,808	(1024, 1024)	16	✓	1	Yellow and Bohai Sea	1	H8/9	X	-	✓	X	X
Wu et al. (2024) [39]	193	(2000, 1600)	16	✓	1	Yellow and Bohai Sea	1	H8/9	X	23	✓	X	✓
Bari et al. (2023) [2]	12,744	(661, 691)	3	X	1	Seas around Morocco	1	MeteoSat	X	-	X	✓	X
Mahdavi et al. (2024) [22]	2,208	-	-	✓	1	The Grand Banks	1	GOES	✓	92	X	✓	X
MFogHub (Ours)	68,000	(1024, 1024)	C_{sat}	✓	15	Yellow/Bohai Sea, East Sea, South Sea, Mediterranean, North Sea, Gulf of Alaska, California Current, etc.	6	FY4A, FY4B, GOES16, GOES17, H8/9, MeteoSat	✓	693	✓	✓	✓

early research has predominantly focused on local performance rather than the broader generalizability of models, potentially leading to inaccurate assessments of a method’s genuine capabilities. Furthermore, the reliance on single-region datasets has constrained exploration into the underlying mechanisms of marine fog formation and dissipation.

To address these issues, we introduce the **MFogHub** dataset—the first multi-regional, multi-satellite dataset for global marine fog detection and forecasting. MFogHub contains over 68,000 samples, as shown in Fig. 1, and spans 15 coastal fog-prone regions, consolidating 693 marine fog events. The dataset captures multi-band meteorological data from 6 geostationary satellites. Given the spatiotemporal nature of marine fog, we organize the data samples in a cube-stream structure with dimensions of ‘timestamp-spectral band-latitude-longitude’ to facilitate usability. The minimum time interval is 30 minutes, with a spatial resolution of 1 km and a size of 1024×1024 pixels. Additionally, more than 11,600 samples are meticulously annotated at the pixel level by meteorological experts. We also provide visual statistical analysis to illustrate the sensitivity of marine fog across variations in region, satellite, and spectral band.

Sixteen standard detection and forecasting methods are selected to showcase the capabilities of MFogHub and establish benchmarks. Unlike single-region and single-satellite datasets, our proposed dataset enables a comprehensive and nuanced evaluation across diverse regions and satellites, revealing performance fluctuations across different methods due to regional discrepancies and satellite variations. Moreover, this dataset presents a new challenge in effectively leveraging multi-regional and multi-satellite data to uncover deeper characteristics of marine fog, thereby enhancing performance and advancing both detection and forecasting. Finally, we investigate the effects of spectral bands and the ratio of positive to negative samples on model performance, aiming to provide valuable insights for future research.

The success of AlphaFold3 [1] would not have been possible without decades of foundational research and ex-

tensive datasets on protein structures, such as those provided by the Protein Data Bank (PDB), which enabled AlphaFold3 to train and validate its predictions. Similarly, our MFogHub dataset addresses the critical need for comprehensive, large-scale, and finely annotated data, providing an essential foundation for advancing machine learning models in marine fog detection and forecasting.

Contributions We introduce MFogHub, the first multi-regional (15 coastal regions) and multi-satellite (6 geostationary satellites) dataset for global marine fog detection and forecasting. This dataset is organized with a novel cube-stream structure, enabling efficient use in deep learning. Through experiments, we demonstrate that MFogHub supports comprehensive evaluation of model performance across regional and satellite dimensions, revealing insights into generalizability. Moreover, it provides a unique opportunity to explore multi-regional and multi-satellite data, facilitating the exploration of the complex dynamics of marine fog. We believe that MFogHub lays a crucial foundation for future research at the intersection of machine learning and meteorology.

2. MFogHub

2.1. Multi-regional data collection

Marine fog is a global phenomenon that occurs in coastal areas [2, 21, 25, 37] and extends to polar regions [6, 41], excluding tropical oceans, as long as the necessary temperature and humidity conditions are met. To better handle global marine fog, we extract almost 9.5 million records from all International Comprehensive Ocean-Atmosphere Data Set (ICOADS) [26] data spanning 2015-2024, which clearly observe the presence or absence of marine fog globally. These records are accumulated into a global grid of $0.25^\circ \times 0.25^\circ$ for frequency tallying, followed by statistical analysis and visualization, as illustrated in Fig. 2. The areas in red on the map indicate higher frequencies of marine fog observations in the ICOADS data, while areas in

blue represent lower frequencies. It is evident that maritime navigation is primarily concentrated along coastlines or established shipping routes, which is why this study focuses on coastal areas for marine fog detection and forecasting. Additionally, by applying a 12.8° sliding window across global regions and drawing on previous research [15, 16], we selected 15 coastal regions with high shipping traffic and frequent fog occurrences as the focus of this study. The detailed covering ranges and information of 15 marine regions are provided in Fig. 1 and the Supplementary Materials.

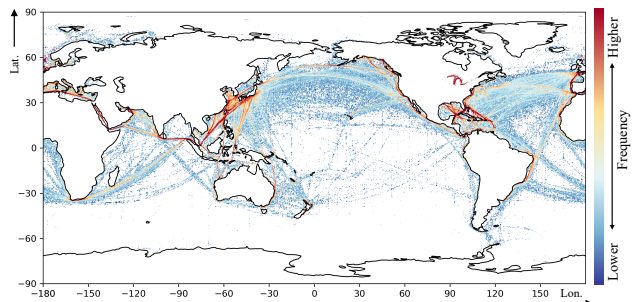


Figure 2. Visualization of marine fog occurrence frequency based on 9.5 million ICOADS observations (2015-2024) for identifying costal fog-prone regions worldwide.

2.2. Multi-satellite data collection

Geostationary satellites, often referred to as the “eyes in the sky,” provide high spatial and temporal resolution data essential for marine fog detection and forecasting. In selecting satellites for this study, we consider two primary factors. First, we prioritize coverage to capture a global perspective of marine fog. To achieve this, we incorporate data from China’s Fengyun (FY)-4A and 4B, Europe’s MeteoSat, and the United States’ GOES-16 and GOES-17 satellites. The second factor is the ability to support multi-satellite studies within the same region. Therefore, we also included Japan’s Himawari (H)-8/9 satellites, which cover regions similar to those of the Fengyun satellites. To improve observational detail and better capture diverse surface features, we utilized multi-spectral L1 data (excluding L1.5 data from MeteoSat) following the projection process. This data includes visible, near-infrared, and far-infrared channels. The primary differences among the data from these satellites lie in the number of spectral bands and their central wavelengths. Additionally, spatial resolution varies across channels, ranging from 500m to 4km. For consistency and comparability, all regional multi-band data were standardized to a spatial resolution of 1km ($\approx 0.0125^\circ$) after projection.

2.3. Cube-stream structure

Marine fog is a dynamically evolving meteorological phenomenon that spans multiple stages, including formation,

maintenance and dissipation. Continuous data samples are especially crucial for forecasting tasks. Thus, to better organize multi-regional, multi-satellite meteorological data for marine fog detection and forecasting, we propose a cube-stream data structure in the MFogHub building upon previous work [14]. As shown in middle part of Fig. 1, each region-satellite data is organized into a cube-stream along with the dimensions of “timestamp-spectral band-latitude-longitude,” represented as $\mathbb{R}^{T \times C \times H \times W}$, where T, C, H, W denotes the number of timestamps, the number of spectral bands, height and width, respectively. Then all cube-stream can be further integrated across different regions and satellites to form the comprehensive MFogHub dataset.

To enable MFogHub to support validation across multiple dimensions, key attributes such as region, satellite, and time are customizable, allowing users to retrieve data that meets specific criteria and assemble custom sub-datasets. Such organization facilitates research into multi-regional and multi-satellite diversity and variation. Furthermore, each cube-stream data across spectral bands is spatio-temporally aligned, enabling flexible slicing operations across multiple dimensions for finer regional data extraction and spectral band sensitivity analysis.

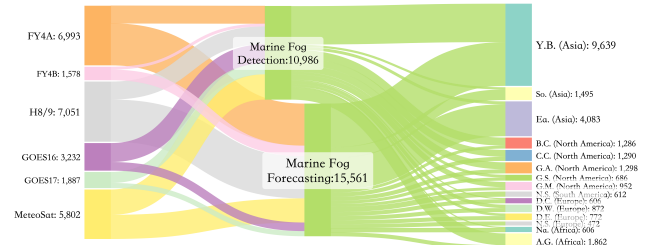


Figure 3. Illustration of data proportion and flow across various regions and satellites for marine fog detection and forecasting in the MFogHub dataset.

Finally, the MFogHub dataset integrates 21 data streams from 6 satellites and comprises 68,000 samples. It illustrates the distribution and flow of data across various satellites, regions, and corresponding tasks within the dataset as shown in the Fig. 3. Based on meteorological reports from various meteorological agencies, 11,600 of these samples are pixel-labeled to indicate the presence or absence of marine fog. Detailed annotation procedures are provided in the Supplementary Materials.

3. Data analysis

3.1. Regional discrepancy

Marine fog distribution varies significantly across regions due to factors such as proximity to land, ocean currents, and other environmental conditions. Using marine fog data and labels from the MFogHub dataset for three regions—Baja

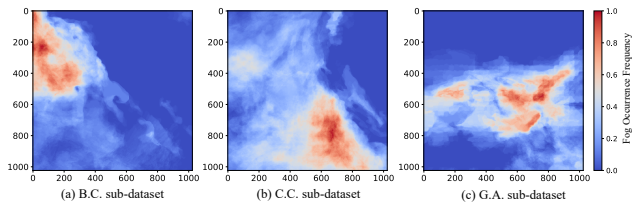


Figure 4. Spatial distribution and intensity variations across B.C., C.C. and G.A. sub-datasets using marine fog detection labels.

190 California (B.C.), California Current (C.C.), and Gulf of
 191 Alaska (G.A.), observed by the GOES-16 satellite—this
 192 study demonstrates how the spatial distribution of marine
 193 fog occurrences differs across regions, as shown in Fig. 4.
 194 In the visualization, regions with redder hues correspond to
 195 higher frequencies of marine fog events.

196 It is clearly evident from the Fig. 4 that each sub-dataset
 197 presents distinct spatial distribution patterns, with signifi-
 198 cant differences in intensity across regions. Additionally,
 199 the visualization reveals that the accumulation patterns of
 200 marine fog events vary between regions: the Baja Cali-
 201 fornia region exhibits more concentrated fog occurrences,
 202 while the other two regions show more dispersed patterns.
 203 These results indicate that the spatial distribution of marine
 204 fog differs notably across regions, posing a significant chal-
 205 lenge to the model’s generalization ability.

206 3.2. Satellite variation

207 Geostationary satellites differ in imaging capabilities due
 208 to variations in spectral bands, spatial resolution, and sub-
 209 satellite points, leading to performance differences in mod-
 210 els trained on data from different satellites for the same re-
 211 gion. Therefore, using the adjacent FengYun-4A (FY4A)
 212 and Himawari-8/9 (H8/9) satellites as examples, we ana-
 213 lyzed marine fog detection data from the Yellow and Bohai
 214 Seas during 2021. We computed pixel histogram distribu-
 215 tions for each spectral band, with the visualized results and
 216 band information shown in Fig. 5. Here, purple and or-
 217 ange figures represent the 14 spectral bands of FY4A and
 218 16 spectral bands of H8/9, respectively.

219 The most evident distinction is that H8/9 has an advan-
 220 tage in the infrared range, while FY4A has more coverage
 221 in the near-infrared. Some key spectral bands overlap be-
 222 tween FY4A and H8/9, though with notable differences.
 223 For example, the band centered around $0.65 \mu\text{m}$ shows a bi-
 224 modal distribution for H8/9 but a unimodal distribution for
 225 FY4A. Additionally, H8/9 has three visible bands, enhanc-
 226 ing its capacity for true-color imaging. These differences
 227 underscore the complementary roles of FY4A and H8/9
 228 in multi-spectral observation and suggest potential benefits
 229 from combining their data for marine fog detection.

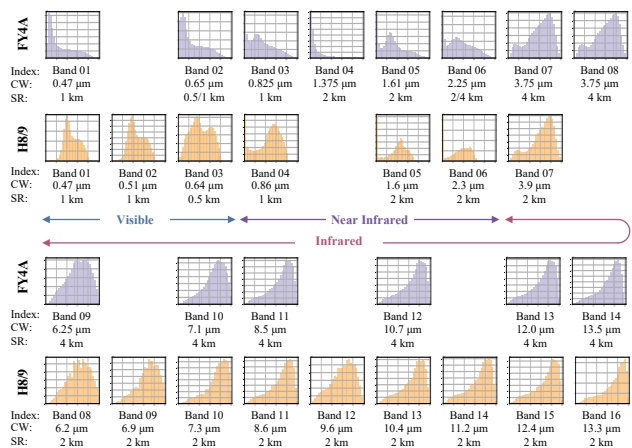


Figure 5. Visualization of pixel histogram distributions and band information (Index, Central Wavelength (CW), and Spatial Resolution (SR)) across multiple bands for FY4A and H8/9 satellites.

3.3. Spectral band sensitivity of marine fog

Due to the varied detection purposes of the satellite imaging instrument’s multiple spectral bands, marine fog exhibits different sensitivities and image characteristics across spectral bands, which can be further reflected in the pixel value distributions. Figure. 5 (A) presents a visualization of pixel histograms for each spectral band image from one marine fog event captured by the FY4A satellite, where the red and colored areas represent the pixel value distributions in fog and non-fog regions across different spectral band, respectively. It can be observed that the pixel distributions across different spectral bands show significant variation, closely linked to the central wavelength of each band.

Firstly, we observe that marine fog primarily exhibits two distinct characteristics across different spectral bands. Specifically, in the visible band ($0.4\text{--}0.7 \mu\text{m}$), as shown in Fig. 6 (b1), water droplets within fog regions strongly scatter sunlight, causing marine fog areas to generally appear as high-brightness regions in the image. In contrast, in the water vapor or infrared bands, as illustrated in Fig. 6 (b2), the water droplets in fog regions have weaker absorption of radiation, resulting in fog areas appearing as low-brightness regions.

Additionally, the separability between marine fog (red areas) and non-fog regions (colored areas) varies across bands, with high separability evident in two specific scenarios. (1) As shown in Fig. 6 (b3), the peak values of marine fog and non-fog regions are clearly separated into distinct pixel value ranges, with a significant mean difference that which are indicated by two dashed lines. (2) As illustrated in Fig. 6 (b4), non-fog pixels exhibit a “bimodal” distribution, whereas fog pixels display a “unimodal” distribution. Finally, based on the previous analysis, we visualized true-

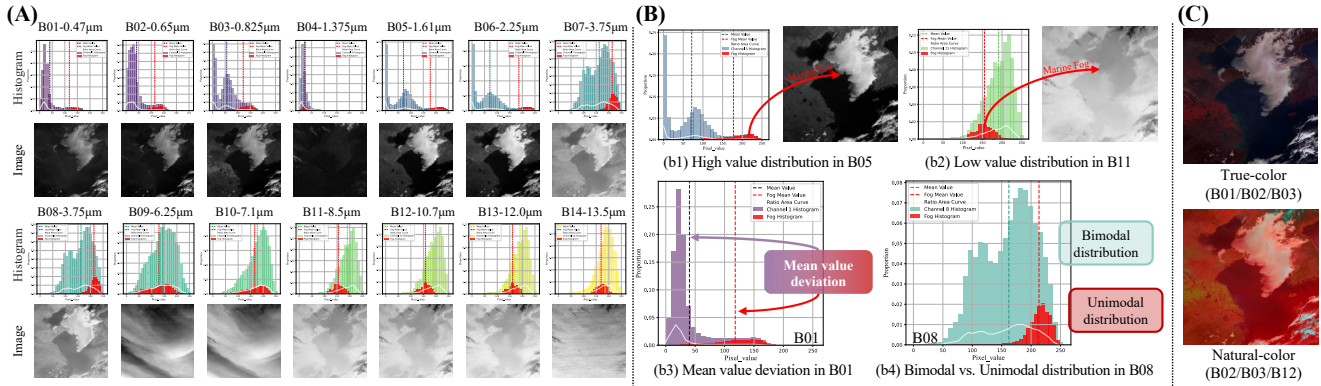


Figure 6. Sensitivity analysis of spectral band for one marine fog event captured by the FY-4A satellite on March 25, 2021. (A) Pixel histogram visualization comparison and single-band images between fog regions (red areas) and non-fog regions (colored areas). (B) Detailed description for characteristics and separability of marine fog area. (C) Synthesized true-color image and natural-color image.

263 color images synthesized from bands B01/B02/B03 and
264 natural-color images synthesized from bands B02/B03/B12
265 as shown in Fig. 6 (C), indicating that the combined use of
266 multiple spectral bands may enhance model performance in
267 distinguishing fog from non-fog regions.

268 4. Experiments

269 In this section, we evaluate the capability of MFogHub
270 to assess the regional and satellite generalization of
271 marine fog models, emphasizing its potential to support multi-
272 region and multi-satellite research. Additionally, we investi-
273 gate the impact of satellite spectral band selection and the
274 positive-to-negative sample ratio on model performance,
275 providing insights for future studies.

276 4.1. Setup

277 **Marine fog detection** involves identifying and delineating
278 marine fog regions from satellite data. Formally, the
279 model is trained to map the input data $\mathcal{X} \in \mathbb{R}^{C \times H \times W}$
280 to a binary mask $\mathcal{M} \in \mathbb{R}^{H \times W}$, where each pixel value $\mathcal{M}_{i,j}$
281 indicates the presence or absence of marine fog at pixel lo-
282 cation (i, j) . Here, C , H , and W represent the number of
283 spectral bands, and the latitude and longitude dimensions of
284 a single data sample, respectively.

285 **Marine fog forecasting** involves predicting future im-
286 age sequences based on historical images. Formally, the
287 model is trained to map a sequence of data samples $\mathcal{X}^{t,T} \in \mathbb{R}^{T \times C \times H \times W}$, where T , C , H , and W represent the tem-
288 poral length, spectral bands, latitude, and longitude, respec-
289 tively, to a future sequence $\mathcal{Y}^{t+1,T'} \in \mathbb{R}^{T' \times C \times H \times W}$.

291 4.2. Implementation details

292 **Detection baselines and metrics.** Eight baseline models
293 are selected for marine fog detection, including CNN-based

architectures (Deeplabv3+ [4], UNet [27], UNet++ [44]),
294 ViT-based architectures (ViT [5], DlinkViT [40]), hybrid
295 structures (Unetformer [9]) and remote sensing methods:
296 (BANet [34], ABCNet [18]). To evaluate their performance
297 on the MFogHub dataset, we used the following metrics:
298 Critical Success Index (CSI), recall, precision, Mean Accu-
299 racy (mAcc), and Mean Intersection over Union (mIoU).

301 **Forecasting baselines and metrics.** Eight forecasting
302 models are selected and categorized into two main types,
303 following OpenSTL [32]. One category consists of
304 recurrent-based methods, including ConvLSTM [28], Pre-
305 dRNN [35], MIM [36], and PhyDNet [7], while the other
306 category includes recurrent-free methods such as SimVP
307 v2 [30], Uniformer [17], VAN [11], and TAU [31]. In
308 addition to standard performance evaluation metrics such
309 as Mean Squared Error (MSE) and Mean Absolute Error
310 (MAE), we also used Structural Similarity Index Measure
311 (SSIM) and Peak Signal-to-Noise Ratio (PSNR) [38] to as-
312 sess the forecasting models.

313 4.3. Assessment of Regional Generalization

314 We present quantitative results for detection baseline mod-
315 els across diverse marine fog regions using data from the
316 Baja California (B.C.), California Current (C.C.), and Gulf
317 of Alaska (G.A.) regions, with evaluation metrics detailed
318 in Table 2. Significant performance variations are observed
319 across these sub-regions, demonstrating the effectiveness of
320 MFogHub in assessing the regional generalization of mod-
321 els. Specifically, DlinkViT [40] and ABCNet [18] show
322 relatively high performance in both the C.C. and G.A. re-
323 gions, with C.C. being easier and G.A. more challenging.
324 However, both models exhibit average performance in the
325 B.C. region. In contrast, ViT-based models [5, 40] per-
326 form exceptionally well in both B.C. and G.A., but their
327 performance is weaker on the simpler C.C. dataset. Even

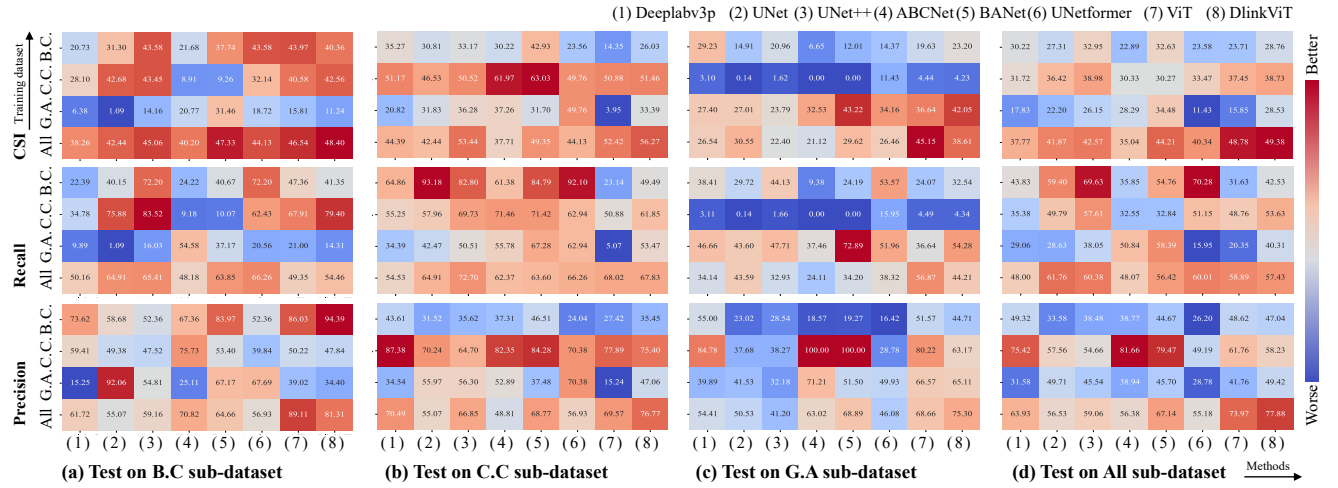


Figure 7. Multi-region evaluation of CSI, Recall and Precision metrics for eight baseline models in marine fog detection, on B.C., C.C., G.A. sub-dataset and all of them, using GOES satellite data. (a)-(d) represents testing on which sub-dataset. Each sub-figure shows rows representing training regions and columns representing model types.

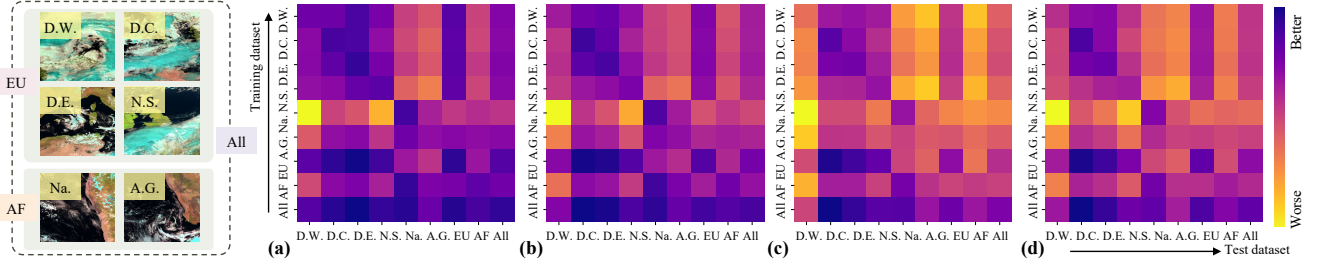


Figure 8. Performance evaluation heatmaps for forecasting using TAU [31] method on different training and test datasets across (a) MSE, (b) MAE, (c) SSIM and (d) PSNR metrics, with single-region (D.W., D.C., D.E., N.S., Na. and A.G.), and multi-regional sub-dataset (European (EU), African (AF) and All).

the regional generalization experiments. The ranking of models differs notably between the two satellites, reflecting the influence of satellite data characteristics on performance. Notably, on the FY4A satellite, SimVP-v2 [30] outperforms TAU [31], MIM [36], and PredRNN [35], securing first place. These results highlight MFogHub's effectiveness in assessing satellite generalization across different models. Furthermore, the H8/9 satellite data consistently yields better results, attributed to its additional spectral bands, reinforcing the value of multi-spectral data in improving model performance.

4.5. Multi-regional research

Multi-region data encompass greater diversity, offering potential benefits for marine fog detection and forecasting tasks. Due to variations in the number of channels across different satellites, this study focuses on multi-region data from a single satellite. We evaluate multiple baseline models using both single-region and multi-region datasets for

both tasks to assess the impact of multi-region data.

For the marine fog detection task, we train eight baseline models on GOES satellite data from individual regions (B.C., C.C., G.A.), as well as from their combined datasets. The models are evaluated using CSI, recall, and precision metrics, with the multi-region results visualized in Fig. 7. The results show that, when focusing on single regions, models trained and tested on the same region perform best, indicating that training on region-specific data enables better capture of local features. Cross-region evaluations highlight a domain gap, leading to performance drops. However, models trained on multi-region data consistently outperform those trained on single regions, particularly for region B.C. This suggests that incorporating additional regions into the training process enhances model generalization and stability. Notably, among the baseline models, simpler architectures and ViT-based models show the most promise for multi-region training.

For the forecasting task, we extended our datasets

367
368
369
370
371
372
373
374
375
376
377
378
379
380
381
382
383
384
385
386
387
388
389
390
391
392
393
394
395
396
397
398
399
400
401
402
403

Table 6. Performance comparison of marine fog detection task between true-color and natural-color images.

		True color images				Natural color images			
		CSI ↑	Recall ↑	mIoU ↑	mAcc ↑	CSI ↑	Recall ↑	mIoU ↑	mAcc ↑
H8/9	UNet [27]	41.95	69.46	59.12	78.79	51.22	74.36	70.67	84.62
	Unetformer [9]	53.08	75.44	67.04	83.03	52.40	74.97	72.80	85.67
	VIT [5]	51.98	74.84	67.46	83.17	57.39	77.70	72.32	85.67
	DlinkVIT [40]	51.27	74.49	65.02	82.01	58.10	78.01	77.55	88.15
FY4A	UNet [27]	37.55	67.16	53.46	75.94	50.81	74.25	65.28	82.11
	Unetformer [9]	51.38	74.59	63.41	81.27	54.15	76.04	67.21	83.16
	VIT [5]	49.40	73.52	63.19	81.08	53.17	75.44	71.12	84.94
	DlinkVIT [40]	50.06	73.93	60.37	79.81	54.84	76.35	70.63	84.78

by combining six individual regions from Meteo satellite data into larger European, African, and all-mixed-region datasets, resulting in nine training-test sets. The results for the TAU method [31], evaluated using MSE, MAE, SSIM, and PSNR metrics, are visualized in Fig. 8. Similar patterns emerge across these four metrics: models trained on closely related multi-region data (e.g., combined European regions) outperform those trained on single regions. This suggests that spatially proximate data are more valuable for improving prediction performance in single-region tasks.

In summary, the results from both detection and forecasting tasks demonstrate the significant benefits of incorporating multi-region data for model generalization. This highlights the potential of MFogHub to serve as a valuable datasets for developing robust marine fog models that can generalize across various regions and satellite platforms.

4.6. Discussions

Impact of different spectral band combinations on model performance. Building on our analysis of fog sensitivity for each band in Sec. 3, we further investigate the role of various spectral bands in marine fog detection by constructing true-color (using the first three channels) and natural-color images (composed of the $0.64\mu\text{m}$, $0.86\mu\text{m}$, and $3.9\mu\text{m}$ bands) through different band combinations. Using satellite data from the H8/9 and FY4A satellites as examples, the image synthesis method and data are illustrated in Fig. 5 (c). Four baseline models [5, 9, 27, 40] are selected to evaluate how different band combinations impact marine fog detection within the same model architecture. The results indicate that natural-color images outperform true-color images, as shown by the pink shading in the table. This suggests that bands with greater pixel distribution differences between fog and non-fog areas are more valuable for fog detection, particularly when working with limited-channel configurations. However, as demonstrated in Table 4, models utilizing all available bands outperform those using any three-band combination, implying that the full-band data may contain additional inter-relationships that are beneficial for marine fog detection.

Impact of positive-to-negative sample ratios. Marine fog is a seasonal phenomenon with irregular occurrences,

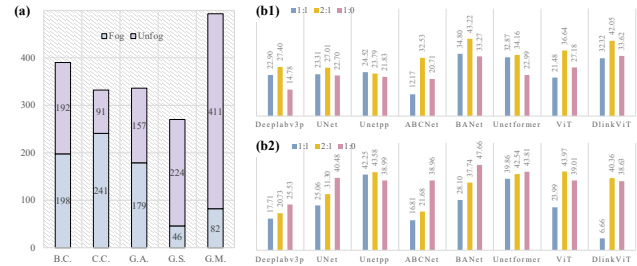


Figure 9. (a) Proportion of positive and negative samples across different regions from GOES satellite. (b1) and (b2) comparison of model performance under varying pos-neg ratios (1:1, 2:1, 1:0) in B.C. and G.A. sub-dataset with CSI metric, respectively.

leading to significant variation in the positive-to-negative sample ratios across different regions during dataset collection. For example, in the five offshore regions captured by the GOES satellite (as shown in Fig. 9 (a)), the Gulf of Mexico (G.M.) sub-dataset has the lowest proportion of positive samples, while the B.C. and G.A. sub-datasets maintain a 1:1 ratio. Based on this, we design three training settings for the B.C. and G.A. sub-datasets, with positive-to-negative sample ratios of 1:1, 2:1, and 1:0, while keeping the number of positive samples constant across all training sets. We then evaluate model performance on a common validation set. The results, specifically in terms of the CSI metric (see Fig. 9 (b1) and (b2)), indicate that different negative sample ratios affect model training to varying degrees; additional metrics, such as recall and precision, are provided in the supplementary materials. Notably, Unet++ [44] demonstrated stable performance across different negative sample ratios, indicating strong robustness against negative sample disturbances. Based on the results from both regions, we recommend a positive-to-negative sample ratio of 2:1 for future dataset construction. This ratio strikes a favorable balance between missed detections and false alarms, making it particularly suitable for marine fog monitoring tasks.

5. Conclusions

In this work, we introduce MFogHub, the most comprehensive, publicly available dataset for global, multi-regional, and multi-satellite marine fog detection and forecasting to date. MFogHub comprises 68,000 data samples from 15 coastal regions prone to marine fog, collected from six geostationary satellites. The data is organized in a “cube-stream” format, consisting of 21 streams in total. Extensive experiments have demonstrated that MFogHub can assess the impact of regional and satellite differences on model performance, while also supports leveraging regional diversity to enhance the model’s representation capabilities. We hope MFogHub will bridge natural sciences and AI, driving both technological and practical advancements.

482

References

483

- [1] Josh Abramson, Jonas Adler, Jack Dunger, Richard Evans, Tim Green, Alexander Pritzel, Olaf Ronneberger, Lindsey Willmore, Andrew J. Ballard, Joshua Bambrick, Sebastian W. Bodenstein, David A. Evans, Chia-Chun Hung, Michael O'Neill, David Reiman, Kathryn Tunyasuvanakool, Zachary Wu, Akvilé Žemgulytė, Eirini Arvaniti, Charles Beattie, Ottavia Bertolli, Alex Bridgland, Alexey Cherepanov, Miles Congreve, Alexander I. Cowen-Rivers, Andrew Cowie, Michael Figurnov, Fabian B. Fuchs, Hannah Gladman, Rishabh Jain, Yousuf A. Khan, Caroline M. R. Low, Kuba Perlin, Anna Potapenko, Pascal Savy, Sukhdeep Singh, Adrian Stecula, Ashok Thillaisundaram, Catherine Tong, Sergei Yakneen, Ellen D. Zhong, Michal Zielinski, Augustin Žídek, Victor Bapst, Pushmeet Kohli, Max Jaderberg, Demis Hassabis, and John M. Jumper. Accurate structure prediction of biomolecular interactions with alphafold 3. *Nature*, 630(8016):493—500, 2024. 2
- [2] Driss Bari, Nabila Lasri, Rania Souri, and Redouane Lguensat. Machine learning for fog-and-low-stratus nowcasting from meteosat seviri satellite images. *Atmosphere*, 14(6):953, 2023. 1, 2
- [3] Huang Bin, Wu Ming, Zhu Shuyue, Zhao Wei, Cui Zhanbei, and LYU Cheng. Sea fog monitoring method based on deep learning satellite multi-channel image fusion (in chinese). *Meteorological Science and Technology*, 49(6):823–829, 2021. 1, 2
- [4] Liang-Chieh Chen, Yukun Zhu, George Papandreou, Florian Schroff, and Hartwig Adam. Encoder-decoder with atrous separable convolution for semantic image segmentation. In *Proceedings of the European conference on computer vision (ECCV)*, pages 801–818, 2018. 5, 6
- [5] Alexey Dosovitskiy, Lucas Beyer, Alexander Kolesnikov, Dirk Weissenborn, Xiaohua Zhai, Thomas Unterthiner, Mostafa Dehghani, Matthias Minderer, Georg Heigold, Sylvain Gelly, et al. An image is worth 16x16 words: Transformers for image recognition at scale. *arXiv preprint arXiv:2010.11929*, 2020. 5, 6, 8
- [6] Gaëlle F Gilson, Hester Jiskoot, Soukeyna Gueye, and John H van Boxel. A climatology of arctic fog along the coast of east greenland. *Quarterly Journal of the Royal Meteorological Society*, 150(759):706–726, 2024. 2
- [7] Vincent Le Guen and Nicolas Thome. Disentangling physical dynamics from unknown factors for unsupervised video prediction. In *Proceedings of the IEEE/CVF conference on computer vision and pattern recognition*, pages 11474–11484, 2020. 5, 6
- [8] Xiaofei Guo, Jianhua Wan, Shanwei Liu, Mingming Xu, Hui Sheng, and Muhammad Yasir. A scse-linknet deep learning model for daytime sea fog detection. *Remote Sensing*, 13(24):5163, 2021. 1
- [9] Ali Hatamizadeh, Ziyue Xu, Dong Yang, Wenqi Li, Holger Roth, and Daguang Xu. Unetformer: A unified vision transformer model and pre-training framework for 3d medical image segmentation. *arXiv preprint arXiv:2204.00631*, 2022. 5, 6, 8
- [10] Ki-Young Heo, Suhyun Park, Kyung-Ja Ha, and Jae-Seol Shim. Algorithm for sea fog monitoring with the use of information technologies. *Meteorological Applications*, 21(2):350–359, 2014. 1
- [11] Jun-Ting Hsieh, Bingbin Liu, De-An Huang, Li F Fei-Fei, and Juan Carlos Niebles. Learning to decompose and disentangle representations for video prediction. *Advances in neural information processing systems*, 31, 2018. 5, 6
- [12] Bin Huang, Shi-bo Gao, Run-ling Yu, Wei Zhao, and Guanbo Zhou. Monitoring sea fog over the yellow sea and bohai bay based on deep convolutional neural network. *Journal of Tropical Meteorology*, 30(3):223–229, 2024. 1
- [13] Yixiang Huang, Ming Wu, Xin Jiang, Jiaao Li, Mengqiu Xu, Chuang Zhang, and Jun Guo. Weakly supervised sea fog detection in remote sensing images via prototype learning. *IEEE Transactions on Geoscience and Remote Sensing*, 2023. 1, 2
- [14] Spyridon Kondylatos, Ioannis Prapas, Gustau Camps-Valls, and Ioannis Papoutsis. Mesogeos: A multi-purpose dataset for data-driven wildfire modeling in the mediterranean. *Advances in Neural Information Processing Systems*, 36, 2024. 3
- [15] Darko Koračin and Clive E Dorman. *Marine fog: challenges and advancements in observations, modeling, and forecasting*. Springer, 2017. 1, 3
- [16] Darko Koračin, Clive E Dorman, John M Lewis, James G Hudson, Eric M Wilcox, and Alicia Torregrosa. Marine fog: A review. *Atmospheric research*, 143:142–175, 2014. 1, 3
- [17] Kunchang Li, Yali Wang, Junhao Zhang, Peng Gao, Guan-glu Song, Yu Liu, Hongsheng Li, and Yu Qiao. Uniformer: Unifying convolution and self-attention for visual recognition. *IEEE Transactions on Pattern Analysis and Machine Intelligence*, 2023. 5, 6
- [18] Rui Li, Shunyi Zheng, Ce Zhang, Chenxi Duan, Libo Wang, and Peter M Atkinson. Abcnet: Attentive bilateral contextual network for efficient semantic segmentation of fine-resolution remotely sensed imagery. *ISPRS Journal of Photogrammetry and Remote Sensing*, 181:84–98, 2021. 5, 6
- [19] Tao Li, Wei Jin, Randi Fu, and Caifen He. Daytime sea fog monitoring using multimodal self-supervised learning with band attention mechanism. *Neural Computing and Applications*, 34(23):21205–21222, 2022. 1, 2
- [20] He Lu, Yi Ma, Shichao Zhang, Xiang Yu, and Jiahua Zhang. Daytime sea fog identification based on multi-satellite information and the eca-transunet model. *Remote Sensing*, 15(16):3949, 2023. 1
- [21] Sahel Mahdavi, Meisam Amani, Terry Bullock, and Steven Beale. A probability-based daytime algorithm for sea fog detection using goes-16 imagery. *IEEE Journal of Selected Topics in Applied Earth Observations and Remote Sensing*, 14:1363–1373, 2020. 1, 2
- [22] Sahel Mahdavi, Meisam Amani, Terry Bullock, and Steven Beale. Enhanced oceanic fog nowcasting through satellite-based recurrent neural networks. *Big Earth Data*, pages 1–20, 2024. 1, 2
- [23] XU Mengqiu, WU Ming, GUO Jun, Chuang Zhang, WANG Yubo, and MA Zhanyu. Sea fog detection based on unsupervised domain adaptation. *Chinese Journal of Aeronautics*, 35(4):415–425, 2022. 1

- 597 [24] Saverio Teodosio Nilo, Filomena Romano, Jan Cermak,
598 Domenico Cimini, Elisabetta Ricciardelli, Angela Cer-
599 sismo, Francesco Di Paola, Donatello Gallucci, Sabrina
600 Gentile, Edoardo Geraldì, et al. Fog detection based on
601 meteosat second generation-spinning enhanced visible and in-
602 frared imager high resolution visible channel. *Remote Sens-*
603 *ing*, 10(4):541, 2018. 1, 2
- 604 [25] Jinhyeok Park, Young Jae Lee, Yongwon Jo, Jaehoon
605 Kim, Jin Hyun Han, Kuk Jin Kim, Young Taeg Kim, and
606 Seoung Bum Kim. Spatio-temporal network for sea fog fore-
607 casting. *Sustainability*, 14(23):16163, 2022. 1, 2
- 608 [26] Research Data Archive, Computational and Information Sys-
609 tems Laboratory, National Center for Atmospheric Research,
610 University Corporation for Atmospheric Research, Physi-
611 cal Sciences Laboratory, Earth System Research Laboratory,
612 OAR, NOAA, U.S. Department of Commerce, Cooperative
613 Institute for Research in Environmental Sciences, Univer-
614 sity of Colorado, National Oceanography Centre, University
615 of Southampton, Met Office, Ministry of Defence, United
616 Kingdom, Deutscher Wetterdienst (German Meteorological
617 Service), Germany, Department of Atmospheric Science,
618 University of Washington, Center for Ocean-Atmospheric
619 Prediction Studies, Florida State University, and National
620 Centers for Environmental Information, NESDIS, NOAA,
621 U.S. Department of Commerce. International comprehen-
622 sive ocean-atmosphere data set (icoads) release 3, individual
623 observations, 2016. 2
- 624 [27] Olaf Ronneberger, Philipp Fischer, and Thomas Brox. U-
625 net: Convolutional networks for biomedical image segmen-
626 tation. In *Medical Image Computing and Computer-Assisted
627 Intervention–MICCAI 2015: 18th International Conference,
628 Munich, Germany, October 5–9, 2015, Proceedings, Part III*
629 *18*, pages 234–241. Springer, 2015. 5, 6, 8
- 630 [28] Xingjian Shi, Zhourong Chen, Hao Wang, Dit-Yan Yeung,
631 Wai-Kin Wong, and Wang-chun Woo. Convolutional lstm
632 network: A machine learning approach for precipitation
633 nowcasting. *Advances in neural information processing sys-
634 tems*, 28, 2015. 5, 6
- 635 [29] Sundingkai Su, Mengqiu Xu, Kaixin Chen, Ming Wu, and
636 Chuang Zhang. E2sam: A pipeline for efficiently extending
637 sam’s capability on cross-modality data via knowledge in-
638 heritance. In *2023 British Machine Vision Conference*, 2023.
639 2
- 640 [30] Cheng Tan, Zhangyang Gao, Siyuan Li, and Stan Z Li.
641 Simvp: Towards simple yet powerful spatiotemporal predic-
642 tive learning. *arXiv preprint arXiv:2211.12509*, 2022. 5, 6,
643 7
- 644 [31] Cheng Tan, Zhangyang Gao, Lirong Wu, Yongjie Xu, Jun
645 Xia, Siyuan Li, and Stan Z Li. Temporal attention unit: To-
646 wards efficient spatiotemporal predictive learning. In *Pro-
647 ceedings of the IEEE/CVF Conference on Computer Vision
648 and Pattern Recognition*, pages 18770–18782, 2023. 5, 6, 7,
649 8
- 650 [32] Cheng Tan, Siyuan Li, Zhangyang Gao, Wenfei Guan, Ze-
651 dong Wang, Zicheng Liu, Lirong Wu, and Stan Z Li. Open-
652 stl: A comprehensive benchmark of spatio-temporal predic-
653 tive learning. In *Conference on Neural Information Process-
654 ing Systems Datasets and Benchmarks Track*, 2023. 5
- [33] JH Wan, Li Jiang, YF Xiao, and Hui Sheng. Sea fog detec-
655 tion based on dynamic threshold algorithm at dawn and dusk
656 time. *The International Archives of the Photogrammetry, Re-
657 mote Sensing and Spatial Information Sciences*, 42:159–163,
658 2019. 1
- [34] Libo Wang, Rui Li, Dongzhi Wang, Chenxi Duan, Teng
660 Wang, and Xiaoliang Meng. Transformer meets convolution:
661 A bilateral awareness network for semantic segmentation of
662 very fine resolution urban scene images. *Remote Sensing*, 13
663 (16):3065, 2021. 5, 6
- [35] Yunbo Wang, Mingsheng Long, Jianmin Wang, Zhifeng
664 Gao, and Philip S Yu. Predrnn: Recurrent neural networks
665 for predictive learning using spatiotemporal lstms. *Advances
666 in neural information processing systems*, 30, 2017. 5, 6, 7
- [36] Yunbo Wang, Jianjin Zhang, Hongyu Zhu, Mingsheng Long,
667 Jianmin Wang, and Philip S Yu. Memory in memory:
668 A predictive neural network for learning higher-order non-
669 stationarity from spatiotemporal dynamics. In *Proceedings
670 of the IEEE/CVF conference on computer vision and pattern
671 recognition*, pages 9154–9162, 2019. 5, 6, 7
- [37] Yu Wang, Zhongfeng Qiu, Dongzhi Zhao, Md Arfan Ali,
672 Chenyue Hu, Yuanzhi Zhang, and Kuo Liao. Automatic de-
673 tection of daytime sea fog based on supervised classification
674 techniques for fy-3d satellite. *Remote Sensing*, 15(9):2283,
675 2023. 2
- [38] Zhou Wang, Alan C Bovik, Hamid R Sheikh, and Eero P Si-
676 moncelli. Image quality assessment: from error visibility to
677 structural similarity. *IEEE transactions on image processing*,
678 13(4):600–612, 2004. 5
- [39] Nan Wu and Wei Jin. Deep spatial–spectral difference net-
679 work with heterogeneous feature mutual learning for sea fog
680 detection. *International Journal of Applied Earth Observa-
681 tion and Geoinformation*, 133:104104, 2024. 1, 2
- [40] Haotian Yan, Sundingkai Su, Ming Wu, Mengqiu Xu, Yi-
682 hao Zuo, Chuang Zhang, and Bin Huang. Seamae: Masked
683 pre-training with meteorological satellite imagery for sea fog
684 detection. *Remote Sensing*, 15(16):4102, 2023. 5, 6, 8
- [41] Li Yi, King-Fai Li, Xianyao Chen, and Ka-Kit Tung. Arctic
685 fog detection using infrared spectral measurements. *Journal
686 of Atmospheric and Oceanic Technology*, 36(8):1643–1656,
687 2019. 2
- [42] Junghee Yun and Kyung-Ja Ha. Physical processes in sea
688 fog formation and characteristics of turbulent air-sea fluxes at
689 socheongcho ocean research station in the yellow sea. *Fron-
690 tiers in Marine Science*, 9:825973, 2022. 1
- [43] Yuan Zhou, Keran Chen, and Xiaofeng Li. Dual-branch neu-
691 ral network for sea fog detection in geostationary ocean color
692 imager. *IEEE Transactions on Geoscience and Remote Sens-
693 ing*, 60:1–17, 2022. 1, 2
- [44] Zongwei Zhou, Md Mahfuzur Rahman Siddiquee, Nima
694 Tajbakhsh, and Jianming Liang. Unet++: Redesigning skip
695 connections to exploit multiscale features in image segmen-
696 tation. *IEEE transactions on medical imaging*, 39(6):1856–
697 1867, 2019. 5, 6, 8